

NANOFLARE ACTIVITY IN THE SOLAR CHROMOSPHERE

D. B. JESS¹, M. MATHIOUDAKIS¹, P. H. KEYS^{1,2}¹Astrophysics Research Centre, School of Mathematics and Physics, Queen's University Belfast, Belfast BT7 1NN, UK and²Solar Physics and Space Plasma Research Centre (SP²RC), University of Sheffield, Hicks Building, Hounsfield Road, Sheffield S3 7RH, UK

ABSTRACT

We use ground-based images of high spatial and temporal resolution to search for evidence of nanoflare activity in the solar chromosphere. Through close examination of more than 1×10^9 pixels in the immediate vicinity of an active region, we show that the distributions of observed intensity fluctuations have subtle asymmetries. A negative excess in the intensity fluctuations indicates that more pixels have fainter-than-average intensities compared with those that appear brighter than average. By employing Monte Carlo simulations, we reveal how the negative excess can be explained by a series of impulsive events, coupled with exponential decays, that are fractionally below the current resolving limits of low-noise equipment on high-resolution ground-based observatories. Importantly, our Monte Carlo simulations provide clear evidence that the intensity asymmetries cannot be explained by photon-counting statistics alone. A comparison to the coronal work of Terzo et al. (2011) suggests that nanoflare activity in the chromosphere is more readily occurring, with an impulsive event occurring every ~ 360 s in a $10\,000\text{ km}^2$ area of the chromosphere, some 50 times more events than a comparably sized region of the corona. As a result, nanoflare activity in the chromosphere is likely to play an important role in providing heat energy to this layer of the solar atmosphere.

Subject headings: methods: numerical — Sun: activity — Sun: chromosphere — Sun: flares

1. INTRODUCTION

Magnetic reconnection is a common phenomenon within the solar atmosphere. Its presence is often observed through explosive events such as solar flares, where extreme localized heating is generated through the conversion of magnetic energy (Priest 1986; Priest & Schrijver 1999). Large-scale flare events can be dramatic, often releasing in excess of 10^{31} ergs of energy during a single event. However, the relative rarity of these phenomena means that they cannot provide the necessary sustained heating to maintain the multi-million degree temperatures observed in the outer solar atmosphere. Instead, it has been suggested that nanoflares, with an energy of approximately 10^{24} ergs, may occur with such regularity in the vicinity of active regions that they can provide a basal background heating (Parker 1988). Previous work on nanoflare heating has focused on coronal observations and modelling, with spectroscopic techniques used to investigate the scaling between the emission measure and the temperature of coronal plasma (e.g., Klimchuk & Cargill 2001; Bradshaw et al. 2012). These results tentatively suggest that nanoflare heating may be responsible for a significant fraction of the energy deposited in the outer solar atmosphere. However, the reliability of these techniques hinge on the accuracy of the emission measure diagnostics as well as the number of optically-thin magnetic strands superimposed along an observational line-of-sight. Indeed, recent work by Cirtain et al. (2013), who employed the high-resolution sounding-rocket imager Hi-C, found a wealth of fine-scale coronal structuring that is below the diffraction limit of current space-based coronal observatories during the instrument's 5-minute flight. To avoid the emission measure sensitivities to local plasma temperatures, Terzo et al. (2011) employed direct imaging techniques and undertook a statistical study utilising X-ray data collected by the X-Ray Telescope (XRT; Golub et al. 2007) onboard Hinode, to investigate whether the analysis of millions of pixels as a single collective could refute or verify the presence of

nanoflares in the Sun's corona. The authors detected a small asymmetry in the measured intensity fluctuations, which they interpreted as the signature of cooling plasma induced by a sequence of impulsive reconnection events. Consequently, Terzo et al. (2011) suggested that nanoflares are a universal heating process within solar active regions. Unfortunately the signal-to-noise, frame rate, and spatial resolution of the observations were not sufficient to unequivocally determine the presence of nanoflare activity and evaluate the specific role they play in the heating of the Sun's outermost atmosphere.

While the majority of recent nanoflare studies have been dedicated to coronal emission, it is the solar chromosphere that provides more tantalising prospects for rapid advancements in solar physics. In the current era we have numerous observational facilities at our disposal that provide a wealth of high spatial, spectral and temporal resolution chromospheric observations. Such observatories include the ground-based Dunn and Swedish Solar Telescopes equipped with the ROSA (Jess et al. 2010c) and CRISP (Scharmer et al. 2008) instruments, respectively, alongside the space-based Hinode satellite. Of particular note is the recently launched Interface Region Imaging Spectrograph (De Pontieu et al. 2014), which aims to bridge the gap between traditional optical observations of the chromosphere and their corresponding coronal EUV counterparts. Even though the chromosphere is only heated to a few thousand degrees above the corresponding photospheric layer, the high densities found within the chromosphere require 2–3 times more energy input to maintain its temperature when compared to the multi-million degree coronal plasma (Withbroe & Noyes 1977; Anderson & Athay 1989). Recent work has revealed that flare signatures can be contained within the chromospheric layer, supporting a wealth of low-lying impulsive events including Ellerman bombs and $H\alpha$ microflares (Ding et al. 1999; Chen et al. 2001; Jess et al. 2010a; Nelson et al. 2013). Furthermore, flares emit most of their radiative signatures in the optical and UV portion of the electromagnetic spectrum (Neidig 1989; Woods et al. 2006), and as a result, the chromosphere is also

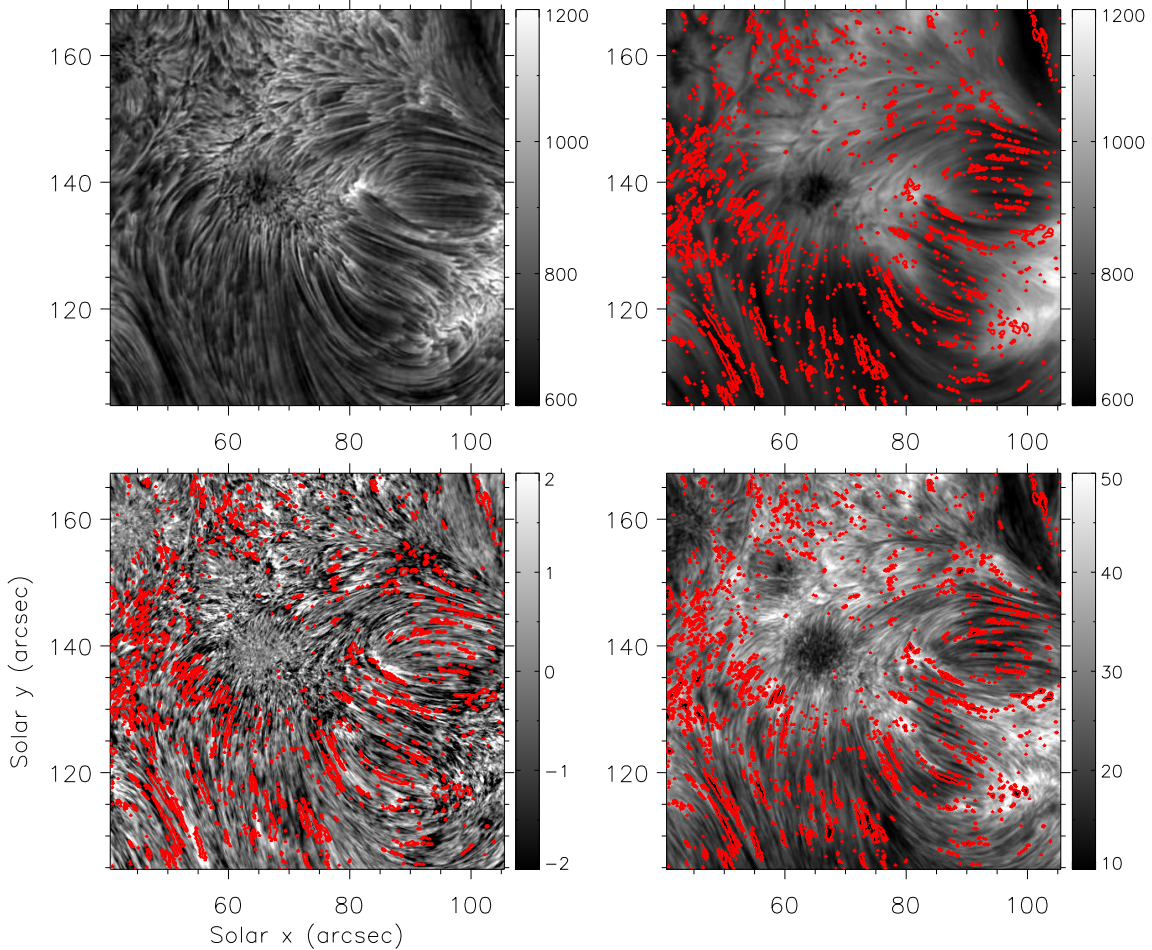


FIG. 1.— An $H\alpha$ core (upper-left) snapshot, acquired at 17:52 UT on 2011 December 10. A time-averaged $H\alpha$ core image (upper-right) is generated by averaging all 4040 individual images acquired during the 2 hour duration of the data set. Colorbars beside the two upper panels denote the image intensities in DN s^{-1} . The lower-left panel displays the time-averaged pixel medians (normalised to their standard deviation, σ , and artificially saturated to assist the clarity of small-scale features), while the lower-right panel displays the standard deviations (in DN s^{-1}) for the entire field-of-view. Red contours outline regions excluded from analysis, and the axis scales are in heliocentric coordinates, where $1'' \approx 725 \text{ km}$. An animation of this figure is available in the online journal.

the primary energy loss region associated with such impulsive events (Fletcher et al. 2011). Thus, the chromosphere presents an ideal, and previously unexplored observational platform to investigate the role nanoflare activity plays in the heating of the Sun’s dynamic atmosphere.

In this paper, we utilise high spatial and temporal resolution observations of the solar chromosphere to investigate whether nanoflare activity can be detected in a relatively quiet active region, devoid of any large scale magnetic activity. We employ a collection of techniques previously used by Terzo et al. (2011), to study the statistics of chromospheric intensity fluctuations, and ultimately relate the analysis of millions of individual pixels to the detection of nanoflare events.

2. OBSERVATIONS

The observational data presented here are part of a sequence obtained during 17:51 – 19:51 UT on 2011 December 10, with the Dunn Solar Telescope (DST) at Sacramento Peak, New Mexico. The newly-commissioned Hydrogen-Alpha Rapid Dynamics camera (HARDcam; Jess et al. 2012a) imaging system was employed to image a location surrounding active region NOAA 11372, positioned at heliocentric coordinates ($71'', 134''$), or N07.6W04.2 in the conventional heliographic co-ordinate system. HARDcam observations em-

ployed a 0.25 \AA filter centered on the $H\alpha$ line core (6562.8 \AA), and utilized a spatial sampling of $0''.138$ per pixel, providing a field-of-view size of $71'' \times 71''$. During the observations, high-order adaptive optics (Rimmele 2004) were used to correct wavefront deformations in real-time. The acquired images were further improved through speckle reconstruction algorithms (Wöger et al. 2008), utilizing $35 \rightarrow 1$ restorations, resulting in a reconstructed cadence of 1.78 s. Atmospheric seeing conditions remained excellent throughout the time series. However, to ensure accurate co-alignment, narrowband HARDcam images were Fourier co-registered and corrected for atmospheric warping through the application of destretching vectors established from simultaneous broadband reference images (Jess et al. 2007). Sample images, incorporating all image processing steps and including a time-averaged reference image, can be viewed in Figure 1.

3. DATA ANALYSIS & INTERPRETATION

3.1. Observational Time Series

During the two hour duration of the observing sequence, no large scale eruptive phenomena (GOES A-class or above) were observed from the active region under investigation. Examination of a time-lapse movie of HARDcam $H\alpha$ images revealed no large-scale structural re-configurations or periodic

motions associated with spicules (Jess et al. 2012b), fibrils (Morton et al. 2011, 2012), or mottles (Kuridze et al. 2012). This magnetically “locked” configuration is verified through examination of the time-averaged $H\alpha$ image displayed in the upper-right panel of Figure 1. Fine-scale structuring can still readily be observed, even after the images have been averaged over the entire 2 hour (4040 frames) duration of the dataset, indicating a rigid chromospheric canopy with little-to-no periodic motions which would have caused intrinsic blurring in the time-averaged image.

Following the methodology of Terzo et al. (2011), our time series was subjected to data cleaning procedures, including the removal of pixels with excessively low count rates, those affected by macroscopic (i.e., $H\alpha$ microflare; Jess et al. 2010a) brightenings, and those demonstrating slow intensity variations due to the displacement or drift of structures within the field-of-view. The signal-to-noise of the time series was high, mostly attributed to the low dark current provided by the Peltier-cooled back-illuminated CCD (Jess et al. 2010c). An average count rate of 785 DN s^{-1} was present, with the darkest parts of the sunspot umbra and the brightest regions of the chromospheric canopy remaining above 550 DN s^{-1} and below 1550 DN s^{-1} , respectively. The time series signal-to-noise ratio, S/N , can be calculated as $S/N = \mu/\sigma_N$, where μ is the signal mean and σ_N is the standard deviation of the noise under normal observing conditions (Schroeder 2000; Jess et al. 2012c). The image noise will contain contributions from both the detector readout and pixelised photon statistics, with the standard deviation of the former $\sigma_d \approx 4.3 \text{ DN s}^{-1}$ (derived from 4000 consecutive dark frames), while the standard deviation of the latter equated as $\sigma_p = \sqrt{n - \sigma_d^2}$, where n is the individual pixel counts in DN s^{-1} . The total noise contribution is found from $\sigma_N = \sqrt{\sigma_d^2 + \sigma_p^2} = \sqrt{n}$, providing an average observational standard deviation $\approx 28 \text{ DN s}^{-1}$ (lower-right panel of Figure 1). Thus, to estimate the range of S/N values found in the observations, the extreme detector counts of 550 DN s^{-1} and 1550 DN s^{-1} provide a signal-to-noise range of $S/N \approx 23 - 39$. As a result of the high signal-to-noise values, no pixels within the field-of-view were discarded on the basis of poor count statistics. To remove macroscopic variations, a linear fit was performed on individual pixel lightcurves, with pixels removed which had intensities reaching or exceeding 150% of the best-fit line at any time. These accounted for $\approx 0.34\%$ (886 pixels) of the total.

Finally, pixels which displayed long-term intensity variations, caused by either the displacement or drift of the structures present, were removed from the field-of-view. To do this, we assumed that if the fluctuations around the linear fit were completely random, and followed a binomial distribution with 0.5 probability of crossing the line-of-best-fit at any time, then the number of crossings due to structural displacements and/or drifts should be smaller than the standard deviation of the binomial distribution (Terzo et al. 2011). As a result, all pixels were removed which had intensities that crossed the line-of-best-fit less than $\sqrt{(m-1)}/2$ times, where m is the number of data points. Thus, for our 2 hour time series incorporating 4040 individual time stamps, all pixels were discarded where their respective lightcurves crossed the best-fit line less than 32 times. These pixels cover $\approx 0.34\%$ (891 pixels) of the total field-of-view. However, observations acquired in $H\alpha$ may also capture dynamic periodic phenomena, such as spicules, mottles, and fibrils. As mentioned

above, a time-lapse movie of the observations revealed no periodic transverse motions, implying a rigid magnetic configuration is present. However, to remove pixels that contain even the most subtle oscillating structures, we calculated the upper crossing threshold which would arise as a result of features oscillating with the lowest transverse periodicities measured in previous $H\alpha$ studies. A structure oscillating with a transverse periodicity of $\approx 70 \text{ s}$ (Kuridze et al. 2012) would cross the best-fit line twice during a complete oscillation cycle. Thus, over the 2 hour ($\approx 7200 \text{ s}$) duration of the dataset, one would expect ≈ 205 crossings of the best-fit line. This is a gross overestimate, as it assumes that the lifetime of an oscillating $H\alpha$ feature is longer than the 2 hour duration of the dataset. Nevertheless, by neglecting pixels within our field-of-view which cross the best-fit line less than 205 times, we only discard $\approx 2.98\%$ (5477 pixels).

Following the rigorous data cleaning, more than 96.6% of the total number of pixels remained, providing in excess of 1.02×10^9 individual pixels. Regions removed from subsequent analysis are contoured in red in Figure 1. Intensity fluctuations, dI , of the remaining pixels were computed similarly to Terzo et al. (2011),

$$dI(x, y, t) = \frac{I(x, y, t) - I_0(x, y, t)}{\sigma_P(x, y, t)}, \quad (1)$$

where $I(x, y, t)$ is the count rate (DN s^{-1}), $I_0(x, y, t)$ is the value of the linear fit, and $\sigma_P(x, y, t)$ is the photon noise estimated as the standard deviation of the pixel lightcurve with respect to the linear fit, acquired at the spatial position $[x, y]$ and time t . The slopes of best-fit lines for each pixel are very small (0 ± 0.12), and as noted by Terzo et al. (2011), show no preference for increasing or decreasing intensities. Due to each lightcurve being normalised to its own respective best-fit line, a more statistically significant distribution can be obtained by including fluctuations over the entire field-of-view which are not removed by the process of data cleaning. By definition, the mean fluctuation for each pixel is 0. However, the upper-left panel of Figure 2 clearly displays a negative excess in the intensity fluctuations (normalised to σ_P), indicating more pixels have fainter-than-average intensities compared with those that appear brighter than average. Averaged over all pixels that passed the data cleaning criteria, the measured median fluctuation is -0.1160 ± 0.0002 . The upper-right panel of Figure 2 displays the distributions of the median values themselves (normalised to their standard deviation), computed individually at each pixel. Again, there is a preference for the median value to be negative with respect to the mean, indicating the presence of a widespread and real statistical phenomenon. Here, the measured median average for all pixels that passed the data cleaning criteria is -0.4172 ± 0.0008 . These effects can be more easily visualised by displaying the temporally-averaged median values across the entire field-of-view. The lower-left panel of Figure 1 displays these values normalised to their individual standard deviations, σ . Here, more than 63.1% (165 592 pixels) of the field-of-view display negative medians, with only 33.8% (90 870 pixels) showing median values greater than 0.

The lower-left panel of Figure 1 can be used to reveal important information regarding what types of lightcurves contribute to those pixels displaying highly negative medians. From the definition of this image, it is clear that darker pixels will have median values significantly below the mean value of 0. Therefore, we can select the most negative pixels, and

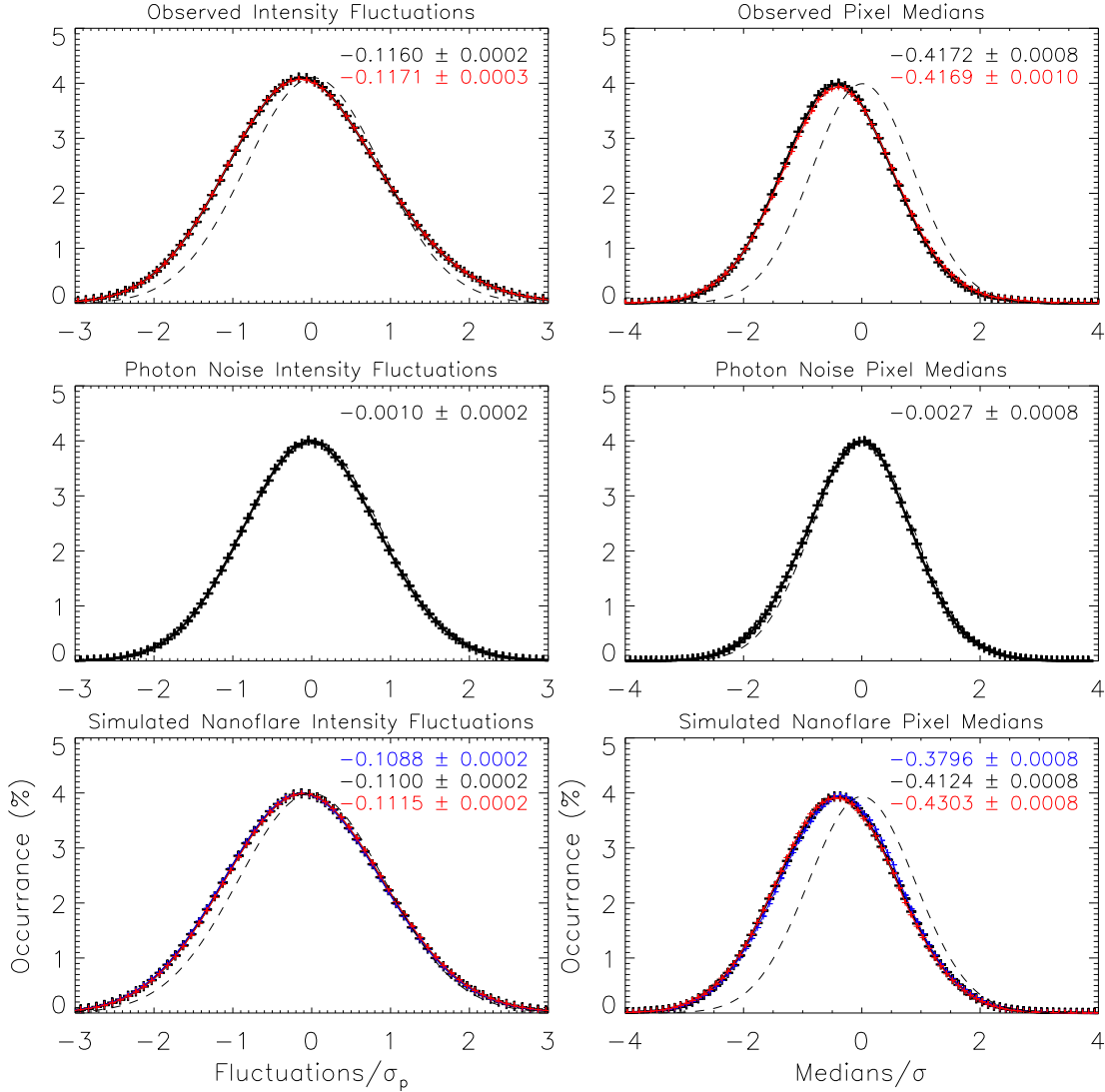


FIG. 2.— The upper-left panel displays the distribution of observed $H\alpha$ pixel intensity fluctuations for the entire field-of-view (red line) and for those which pass the threshold criteria outlined in § 3 (black line), normalized to the photon noise, σ_P . The upper-right panel shows the distribution of median fluctuations, computed individually for each pixel within the entire field-of-view (red line) and those which pass the threshold criteria (black line), both of which are normalized to their standard deviation, σ . The remaining panels are identical to the upper distributions, but created for synthetic data sets which display fluctuations based entirely upon Poisson noise statistics (middle) and Monte Carlo simulations of nanoflare activity ($A = 20 \text{ DN s}^{-1}$, $dt = 360 \text{ s}$; lower). The blue, black and red lines in the lower panels represent e -folding times of $\tau = 37 \text{ s}$, 51 s and 65 s , respectively. For each distribution, a Gaussian centered on zero with unit width is displayed as a dashed line for reference, while the centroid offsets for individual distributions are displayed in the upper-right corner of each panel.

display the resulting lightcurves to examine why their time-averaged median values are so low. The upper panel of Figure 3 displays a 500 s section of a lightcurve that corresponds to a pixel with a median average of -1.575 ± 0.002 when normalised to the standard deviation, or $-7.48 \pm 0.07 \text{ DN s}^{-1}$ in raw units. This lightcurve clearly shows a small-scale impulsive event, with a peak rise in intensity of $\sim 60 \text{ DN s}^{-1}$ above the mean, corresponding to a rise of $\sim 7\%$ above the background. This event is small enough to evade our initial intensity threshold of 50%, which was designed to filter out macroscopic events such as $H\alpha$ microflares, yet large enough to substantially diverge the pixel median from the average value as a result of the impulsive rise and gradual decay. This example is at the extreme end of the median scale. However, smaller impulsive events, which may be difficult, if not impossible to detect by eye, may result in less severe negative medians. A collection of pseudo-random, impulsive events (i.e. nanoflares) that are at, or below the visual detection limit, may be the

cause of the overall distribution asymmetries present in our observations.

Since our filtering thresholds only removed $\approx 3.4\%$ of the total number of pixels, a natural question arises as to what contribution the filtered fluctuations would have on the measured $H\alpha$ distributions displayed in the upper panels of Figure 2. To test the robustness of our methodologies, we generated identical distributions for the entire observational field-of-view (i.e., including all previously discarded pixels). The resulting distributions are overplotted in the upper panels of Figure 2 using solid red lines. Using the entire field-of-view, the observed intensity fluctuations remain in close agreement with those obtained using the filtered image sequence, implying significant robustness in our chosen methodologies. Differences between the respective distributions are incredibly subtle, and most likely difficult to identify by eye. However, there is a fractional increase in the negative offset after including the previously discarded pixels. This is most likely

a consequence of including more macroscopic $H\alpha$ brightenings in the field-of-view, thus causing the separation between the mean and median values to become more pronounced as a result of the longer decay timescales associated with these features ($\sim 3 - 5$ minutes; Jess et al. 2010a). Furthermore, the intensity fluctuation profile itself is marginally broader when compared to the filtered field-of-view. Again, this is likely attributed to the inclusion of more rapidly evolving and/or brightening structures within the field-of-view, thus causing greater amplitude fluctuations to be included in the far wings of the distribution. The observed median fluctuations of the filtered and full fields-of-view have almost identical negative offsets. This is most likely a consequence of larger amplitude $H\alpha$ brightenings having a reduced occurrence rate when compared to nanoflare activity, resulting in the peak median offset being determined solely by the relatively frequent nanoflares. However, as per the intensity fluctuation distribution, the median values of the full field-of-view demonstrate a slightly more broadened profile when compared to the filtered dataset. The often significantly longer decay times associated with large-scale chromospheric brightenings helps to further separate the statistical mean and median values, thus contributing to more negative offsets. Contrarily, rapidly evolving chromospheric features, from either spicule-type transverse oscillations or $H\alpha$ microflare activity with decay times similar to that of a nanoflare (~ 51 s), will help to negate the median offset and thus contribute to more positive values.

Interestingly, while the observed intensity fluctuations (upper-left panel of Figure 2) are predominantly negatively offset, the positive tail of the distribution appears to remain elevated beyond that of the comparative Gaussian centered about zero. This implies a degree of positive skewness to the observed distributions. To quantify this, we calculated the Fisher and Pearson coefficients related to the distribution, finding values of 0.111 and 0.096, respectively. This is a slight degree of skewness, but it implies that small-scale characteristics embedded within the data are promoting a positive skew. Since we set our intensity-filtering threshold to 50% above the line-of-best-fit, some larger impulsive brightenings may still be present in the data (see, e.g., the upper panel of Figure 3). These more-significant impulsive events will result in contributions to larger I/σ_P values, thus causing the positive tails of the distributions to stay elevated over a wider range. To test this theory, we also calculated the Fisher and Pearson coefficients for the distributions incorporating the entire observational field-of-view (i.e., including all previously filtered pixels), with values of 0.115 and 0.099 found, respectively. These marginally inflated values indicate a higher degree of positive skewness when more macroscopic $H\alpha$ brightenings are included in the distribution, thus strengthening our interpretation. Lowering the intensity threshold may help to reduce these extended tails (i.e., the skewness). However, since we believe that nanoflare activity is of a similar magnitude to the Poisson noise statistics, there is a fine line between removing very small-scale H-alpha microflare events (which may contribute to the skewness) and cropping nanoflare activity itself. While the number statistics present in Terzo et al. (2011) are significantly lower than what we present here, a degree of positive skew can also be viewed in their intensity distributions (see, e.g., Figures 4 & 6 of Terzo et al. 2011). The authors do not attempt to interpret this phenomenon, but it is interesting to note that skewness appears to be a feature synonymous with both chromospheric and coronal observations.

3.2. Monte Carlo Simulations

To investigate further, we performed a series of Monte Carlo simulations. Following Terzo et al. (2011), we assumed as a null hypothesis that all pixel fluctuations are solely due to photon noise convolved with an intrinsically flat background. To simulate this, we first created a time-averaged $H\alpha$ image by averaging all 4040 individual frames together. The resulting emission map is shown in the upper-right panel of Figure 1, and forms the basis of our synthetic time series. A new datacube, 4040 frames in duration, is generated with an identical time-averaged emission map occupying each time stamp. Then, we introduce detector noise at each pixel using Poisson statistics which have the same average fluctuation amplitudes that we observed in the real data (lower-right panel of Figure 1). Finally, we apply the same analysis routines to our synthetic dataset, with the resulting intensity fluctuations and pixel medians displayed in the middle-left and middle-right panels, respectively, of Figure 2. Here, the measured median fluctuation is -0.0010 ± 0.0002 , while the median average is -0.0027 ± 0.0008 . Under normal circumstances Poisson statistics introduce an degree of asymmetry to a photon-based distribution as a result of discrete data sampling. However, as the sample size increases, a typical Poisson distribution becomes more Gaussian-like, and as a result, more symmetric. Our synthetic distributions incorporate in excess of 1.02×10^9 individual pixels, and as both measured values are very close to 0, the resulting distributions closely follow the Gaussians of unit width overplotted (dashed line) in the middle panels of Figure 2. Thus, the large negative asymmetries present in the observations cannot be a direct consequence of Poisson statistics alone.

Next, we introduced a series of impulsive rises in intensity, followed by exponential decays, in an attempt to replicate a typical time series dominated by nanoflare activity. We must stress that the physics of a cooling plasma does not necessarily follow a strict exponential decay. In reality, it is a broken power-law distribution with different indices for evaporative and non-evaporative processes, in addition to whether the plasma is conductively or radiatively cooling (Antiochos & Sturrock 1978). However, we chose a more simplistic exponential decay shape to make parameterizing the cooling and constraining the decay time more straightforward. As performed by Terzo et al. (2011), we allowed the impulsive events to be governed by three distinct parameters: the amplitude, A , of the impulsive rise; the e -folding time, τ , of the exponential decay phase; and the average time interval between two successive perturbations, dt . A number of small-scale impulsive events are detectable by eye in pixel lightcurves that display a highly negative median (see, e.g., the upper panel of Figure 3). Measurement of eight individual decay phases provides $\tau \approx 51 \pm 14$ s. This is consistent with the chromospheric work of de Jager (1985), although is much lower than previously used coronal values (360 s; Terzo et al. 2011). The higher electron densities found in the chromosphere would lead to reduced radiative cooling timescales (Pallavicini et al. 1990), hence explaining the difference in the value of τ between chromospheric and coronal observations. Alternatively, the different values of τ could be a direct consequence of the spatial resolution. A smaller structure may be expected to evolve on faster timescales when compared to a more sizeable feature. Therefore, one may expect to resolve smaller and faster evolving structures in the high resolution chromospheric images compared to those found in XRT ob-

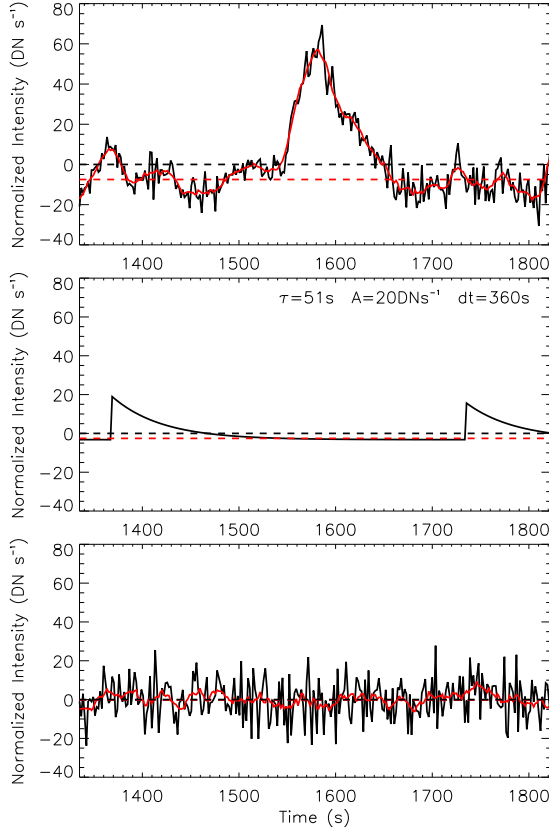


FIG. 3.— A 500 s duration lightcurve (solid black line; upper), taken from a pixel that displays a highly negative median (-1.575 ± 0.002) when normalised to the standard deviation. Identical 500 s duration lightcurves, for a Monte Carlo simulation with parameters $\tau = 51$ s, $A = 20$ DN s^{-1} , and $dt = 360$ s, are displayed without (middle) and with (lower) added photon noise. Nine-point (≈ 16 s) running averages are displayed using solid red lines, while the dashed black and red horizontal lines mark the lightcurve average (0 DN s^{-1}) and median values, respectively. A preference for negative medians exists even when the impulsive amplitudes are lower than the photon noise. The horizontal axes displays time from the start of the observing sequence at 17:51 UT.

servations. For the purposes of our simulations, we fix the e -folding time to equal the value measured in our observations ($\tau = 51$ s).

One of the larger impulsive events that passed through our data cleaning procedures has an amplitude, $A \approx 60$ DN s^{-1} (upper panel of Figure 3). This event is comparatively large, and results in a very low lightcurve median value. As a result, we must choose an impulsive amplitude which is significantly below 60 DN s^{-1} to ensure the average median value over the entire field-of-view is closer to the observational measurement of -0.4172 ± 0.0008 when normalised to the standard deviation, σ . As nanoflares are believed to be at (or below) the current observational detection limit, we can choose an impulsive amplitude similar to the standard deviation of our observational time series, which includes fluctuations due to both detector readout noise and small-scale solar variability. The lower-right image in Figure 1 displays the standard deviations for the entire field-of-view, and clearly shows how regions surrounding the central sunspot have slightly higher standard deviations when compared to those in darker, more distant locations of the chromospheric canopy. The average standard deviation for the entire field-of-view (σ_N) is 28 DN s^{-1} , which is considerably higher than the fluctuations solely due to detector readout noise ($\sigma_d \approx 4$ DN s^{-1}). Em-

ploying the full range of σ_N values ($\approx 23 - 39$ DN s^{-1}), the resulting photon noise can be computed as $\sigma_p = \sqrt{\sigma_N^2 - \sigma_d^2}$. This provides a photon noise estimate in the range of $\sigma_p \approx 23 - 39$ DN s^{-1} , indicating the dominant noise contribution arises directly from photon statistics. However, in addition to traditional shot noise characteristics, we suggest the larger standard deviations found in these locations may also be a direct consequence of larger magnetic field concentrations in these areas giving rise to bigger impulsive events, and hence more intensity variability. Thus, we select a series of average amplitudes, $A = 10, 15, 20$, and 25 DN s^{-1} , and create a random-uniform distribution for each amplitude ranging from 50% to 150% (12.5 – 37.5 DN s^{-1} in the case of $A = 25$ DN s^{-1}), which then forms the selection basis of our impulsive intensity rises. The final parameter is the average time interval between two successive perturbations, dt . In order to compare our Monte Carlo simulations with those computed by Terzo et al. (2011), we selected a range of values, $180 \leq dt \leq 540$ s, where each is separated by 60 s (i.e., $dt = 180, 240, 360, 420, 480$, and 540 s). For each value, a Poisson distribution centred on the chosen dt is generated, which provides a series of successive time intervals between adjacent impulsive events. A Poisson distribution is chosen since each event will be triggered an integer number of frames after the previous one. Impulsive events are then added to the 4040-frame emission map time series, resulting in the average pixel count rates increasing slightly as a result of the perturbations having positive values. To ensure that individual pixels in the simulated time series have an identical mean to that of the actual $\text{H}\alpha$ observations, a constant intensity offset is applied to each pixel to maintain the same time-averaged DN s^{-1} count rates present in the real data.

The resulting 24 time series ($\tau = 51$ s; $A = 10, 15, 20, 25$ DN s^{-1} ; $dt = 180, 240, 360, 420, 480, 540$ s) have non-periodic behaviour, but with low-level impulsive events followed by exponential decreasing trends (middle panel of Figure 3). These lightcurves are then subjected to the addition of photon noise according to our null-hypothesis test above, and re-analysed using our observational routines. An example synthetic lightcurve, with input parameters $\tau = 51$ s, $A = 15$ DN s^{-1} , and $dt = 180$ s, is displayed in the lower panel of Figure 3. The resulting intensity fluctuations and pixel medians for the 24 time series were compared to the observational measurements, with the closest match occurring for the variables $\tau = 51$ s, $A = 20$ DN s^{-1} , and $dt = 360$ s. The lower-left and lower-right panels of Figure 2 display the best-match intensity fluctuation and pixel median distributions. Here, the measured median fluctuation is -0.1100 ± 0.0002 , while the median average is -0.4124 ± 0.0008 .

4. CONCLUDING REMARKS

The methodology presented in this paper is based on the coronal work of Terzo et al. (2011). However, our findings have a number of key differences, with some quantified in Table 1. First, the nanoflare amplitude used in our Monte Carlo simulations produces a substantially smaller scatter in the percentage intensity increases that result from the simulations of nanoflare activity. For our best-fit case, we use a value of 20 DN s^{-1} , which gives an impulsive rise between 1–3% above the brightest and darkest quiescent background pixels, respectively. Terzo et al. (2011) used $A = 60$ DN s^{-1} , which produced a substantially wider range of intensity increases, of the order of 3–200% above their brightest (~ 1700 DN s^{-1}) and darkest (~ 30 DN s^{-1}) quiescent background pixels, re-

TABLE 1
COMPARISON BETWEEN THIS WORK AND THAT OF TERZO ET AL. (2011).

Parameter	Current Study	Terzo et al. (2011)
Observations	Optical ($H\alpha$)	X-Ray (Hinode XRT)
Pixel area	512×512 pixels ²	256×256 pixels ²
Field-of-view	71×71 arcsec ²	256×256 arcsec ²
Time series duration	120 min	26 min
Frames	4040	303
Total pixels	1.06×10^9	1.99×10^7
Total pixels after data cleaning	1.02×10^9	1.11×10^7
Median fluctuation / σ_P (entire FOV)	-0.1160 ± 0.0002	not stated
Median / σ (entire FOV)	-0.4172 ± 0.0008	-0.0258 ± 0.0004
Amplitude (A ; Monte-Carlo best fit)	20 DN s^{-1}	60 DN s^{-1}
e-folding time (τ ; Monte-Carlo best fit)	51 s	360 s
Nanoflare interval (dt ; Monte-Carlo best fit)	360 s	360 s

spectively. This may be a direct consequence of the relatively poor signal-to-noise encountered with faint coronal X-ray observations. Contrarily, the high signal-to-noise of our HARDcam $H\alpha$ observations enables the amplitudes of potential nanoflare activity to be constrained to a much narrower window. Importantly, because the nanoflare amplitude is only marginally below the observational noise threshold, it seems likely that next-generation cameras may be sensitive enough to temporally resolve nanoflare activity, especially if contributions due to dark current and readout noise can be minimised. Secondly, the average cadence between successive nanoflare events that provided the closest resemblance to our $H\alpha$ observations is identical to that used by Terzo et al. (2011). However, while the average cadence, $dt = 360$ s, may be identical, the difference in spatial resolution between the two studies is drastically different. In our current chromospheric simulations, we require a nanoflare event approximately every 360 s over a spatial scale of $\sim 10\,000 \text{ km}^2$ (1 pixel). On the other hand, the coronal simulations of Terzo et al. (2011) required a nanoflare event approximately every 360 s over a spatial scale of $\sim 525\,000 \text{ km}^2$ (1 pixel). This suggests that on comparable spatial scales, there are ~ 50 times more nanoflare events in the solar chromosphere compared to the corona. Thirdly, our observed distributions of intensity fluctuations and pixel medians (upper panels of Figure 2) have a larger negative off-

set than those presented by Terzo et al. (2011). Typically, the lower impulsive amplitudes used in our Monte Carlo simulations would reduce the associated negative offset. However, this effect is negated by the much shorter e -folding time which causes the intensities to drop back down to their quiescent value much more abruptly. As a result, the sensitivity to small-scale impulsive events in the (optical) chromosphere is substantially higher.

Our results suggest that nanoflare activity is readily occurring in the solar chromosphere. The energetics associated with these events are only fractionally below the noise threshold of our time series, and as a result, next-generation instruments with reduced readout noise may actually be able to temporally resolve such impulsive events. Even with a relatively small field-of-view size ($71'' \times 71''$), our Monte Carlo simulations suggest that over 2.5×10^6 impulsive events occur every hour. Thus, we suggest that nanoflare heating may be a significant heating mechanism in the solar chromosphere.

D.B.J. would like to thank STFC for an Ernest Rutherford Fellowship, in addition to a dedicated standard grant which allowed this project to be undertaken. M.M. is grateful to STFC for research support.

Facilities: Dunn (HARDcam).

REFERENCES

- Anderson, L. S., & Athay, R. G., 1989, *ApJ*, 336, 1089
 Antiochos, S. K., & Sturrock, P. A., 1978, *ApJ*, 220, 1137
 Bradshaw, S. J., Klimchuk, J. A., & Reep, J. W., 2012, *ApJ*, 758, 53
 Chen, P.-F., Fang, C., & Ding, M.-D. D., 2001, *ChJAS*, 1, 176
 Cirtain, J. W., Golub, L., Winebarger, A. R., et al., 2013, *Nature*, 493, 501
 de Jager, C., 1985, *Sol. Phys.*, 98, 267
 De Pontieu, B., Title, A. M., Lemen, J. R., et al., 2014, *Sol. Phys.*, 289, 2733
 Ding, M. D., Fang, C., & Yun, H. S., 1999, *ApJ*, 512, 454
 Fletcher, L., Dennis, B. R., Hudson, H. S., et al., 2011, *Space Sci. Rev.*, 159, 19
 Golub, L., Deluca, E., Austin, G., et al., 2007, *Sol. Phys.*, 243, 63
 Jess, D. B., Andić, A., Mathioudakis, M., Bloomfield, D. S., & Keenan, F. P., 2007, *A&A*, 473, 943
 Jess, D. B., De Moortel, I., Mathioudakis, M., Christian, D. J., Reardon, K. P., Keys, P. H., & Keenan, F. P., 2012a, *ApJ*, 757, 160
 Jess, D. B., Mathioudakis, M., Browning, P. K., Crockett, P. J., & Keenan, F. P., 2010a, *ApJ*, 712, L111
 Jess, D. B., Mathioudakis, M., Christian, D. J., Crockett, P. J., & Keenan, F. P., 2010b, *ApJ*, 719, L134
 Jess, D. B., Mathioudakis, M., Christian, D. J., Keenan, F. P., Ryans, R. S. I., & Crockett, P. J., 2010c, *Sol. Phys.*, 261, 363
 Jess, D. B., Pascoe, D. J., Christian, D. J., et al., 2012b, *ApJ*, 744, L5
 Jess, D. B., Shelyag, S., Mathioudakis, M., et al., 2012c, *ApJ*, 746, 183
 Klimchuk, J. A., & Cargill, P. J., 2001, *ApJ*, 553, 440
 Kuridze, D., Morton, R. J., Erdélyi, R., et al., 2012, *ApJ*, 750, 51
 Morton, R. J., Erdélyi, R., Jess, D. B., & Mathioudakis, M., 2011, *ApJ*, 729, L18
 Morton, R. J., Verth, G., Jess, D. B., et al., 2012, *Nature Communications*, 3
 Neidig, D. F., 1989, *Sol. Phys.*, 121, 261
 Nelson, C. J., Doyle, J. G., Erdélyi, R., et al., 2013, *Sol. Phys.*, 283, 307
 Pallavicini, R., Tagliaferri, G., & Stella, L., 1990, *A&A*, 228, 403
 Parker, E. N., 1988, *ApJ*, 330, 474
 Priest, E. R., 1986, *Sol. Phys.*, 104, 1
 Priest, E. R., & Schrijver, K., 1999, *Sol. Phys.*, 190, 1
 Reardon, K. P., Lepreti, F., Carbone, V., & Vecchio, A., 2008, *ApJ*, 683, L207
 Rimmele, T. R., 2004, *Proc. SPIE*, 5490, 34
 Scharmer, G. B., Narayan, G., Hillberg, T., et al., 2008, *ApJ*, 689, L69
 Schroeder, D. J., 2000, *Astronomical optics / Daniel J. Schroeder*. San Diego : Academic Press, c2000
 Terzo, S., Reale, F., Miceli, M., et al., 2011, *ApJ*, 736, 111
 Withbroe, G. L., & Noyes, R. W., 1977, *ARA&A*, 15, 363
 Wöger, F., von der Lühe, O., & Reardon, K., 2008, *A&A*, 488, 375
 Woods, T. N., Kopp, G., & Chamberlin, P. C., 2006, *Journal of Geophysical Research (Space Physics)*, 111, 10